Pervasive Seismic Wave Reflectivity and Metasomatism of the Tonga Mantle Wedge

Yingcai Zheng, *et al.*

Science **316**, 855 (2007);
DOI: 10.1126/science.1138074

Science (print ISSN 0036-8075; online ISSN 1095-9203) is published weekly, except the last week in December, by the American Association for the Advancement of Science, 1200 New York Avenue NW, Washington, DC 20005.

Pervasive Seismic Wave Reflectivity and Metasomatism of the Tonga Mantle Wedge

Yingcai Zheng,[1] Thorne Lay,[1]* Megan P. Flanagan,[2] Quentin Williams[1]

Subduction zones play critical roles in the recycling of oceanic lithosphere and the generation of continental crust. Seismic imaging can reveal structures associated with key dynamic processes occurring in the upper-mantle wedge above the sinking oceanic slab. Three-dimensional images of reflecting interfaces throughout the upper-mantle wedge above the subducting Tonga slab were obtained by migration of teleseismic recordings of underside *P*- and *S*-wave reflections. Laterally continuous weak reflectors with tens of kilometers of topography were detected at depths near 90, 125, 200, 250, 300, 330, 390, 410, and 450 kilometers. *P*- and *S*-wave impedances decreased at the 330-kilometer and 450-kilometer reflectors, and *S*-wave impedance decreased near 200 kilometers in the vicinity of the slab and near 390 kilometers, just above the global 410-kilometer increase. The pervasive seismic reflectivity results from phase transitions and compositional zonation associated with extensive metasomatism involving slab-derived fluids rising through the wedge.

Dipping oceanic lithosphere sinks at subduction zones in a fundamental process of plate tectonics. The overlying mantle wedge becomes enriched in volatiles released from the descending slab, undergoes localized partial melting and ascent of magmas to produce island or continental arcs, and experiences both slab-parallel and slab-perpendicular shear flows, often with back-arc spreading due to the seaward migration of the trench (*1*). Characterizing the structure and processes located in the mantle wedge is essential for understanding the formation of continental crust, evolution of back-arc basins, and volatile circulation in the mantle (*1*, *2*).

For the past 40 million years, the Pacific plate has been sinking at the Tonga subduction zone, the northern portion of which has the highest known rate of interplate convergence due to a combination of fast Pacific plate motion and rapid back-arc spreading of the Lau Basin (*3*). The number of intermediate- and deep-focus earthquakes in the Tonga slab is higher than in other subduction zones, and the seismicity reveals slab buckling and contortions caused by resistance to sinking near the global 660-km-deep seismic discontinuity, accentuated by interactions with lower-mantle flow patterns (*4*). Seismicity also occurs outside of the Tonga slab at depths below 500 km, in what appear to be remnant slab pieces from earlier subduction zones with different geometries (*5*), resulting in a broad horizontal distribution of deep-focus earthquakes.

Investigations of the structure of the mantle wedge above the Tonga slab have mainly used sparse seismic instrument deployments along the island arc and across the Lau Basin to image volumetric *P*- and *S*-wave velocity variations (*6*, *7*), *P*-wave attenuation (*8*), upper-mantle *S*-wave velocity discontinuities inferred from converted wave analyses (*9*, *10*), and *S*-wave splitting patterns (*11*). The data coverage is limited, resolving structure only along a couple of two-dimensional (2D) profiles parallel and perpendicular to the arc. The mantle wedge appears to be structurally complex (requiring a 3D characterization) but, as is true for other island-arc regions, it is prohibitively expensive to deploy large numbers of portable seismic stations above the wedge. We developed a 3D model of *P*- and *S*-wave reflecting interfaces throughout the Tonga mantle wedge using signals from deep Tonga slab earthquakes recorded at teleseismic global seismic stations. The startling extent of seismic reflectivity that we discovered allowed us to place constraints on petrological and dynamical phenomena in the wedge.

Seismic data analysis. Seismic wave investigations tend to focus on either the "smooth" components of internal Earth structure (such as volumetric velocity heterogeneity), which are best resolved by seismic tomography, or the "rough" components (involving strong gradients or discontinuities in material properties), which are best resolved by the stacking of reflected or converted arrivals. Most mantle-wedge studies have addressed smooth components of the structure, revealing broad patterns associated with thermal heterogeneity in the slab and wedge (*12*), but some have resolved the reflectivity of limited locations or sections of mantle wedges (*9*, *10*, *13*, *14*). One strategy for detecting reflecting structures in the wedge involves the analysis of initially up-going energy from deep-focus events that reflects downward from the underside of mantle discontinuities to eventually be observed at teleseismic distances (Fig. 1). This geometry provides high lateral spatial resolution of structure near the source. This strategy has previously been applied to individual events (*15*–*18*), but we exploited the abundant, widespread deep seismicity beneath the Tonga mantle wedge and the global distribution of broadband seismographic stations operated by the Federation of Digital Seismic Networks, regional networks, and EarthScope Transportable Array to generalize it into a multiple-event true-amplitude 3D wavefield migration, stacking signals to determine reflector positions at depth. Essentially, we turned standard reflection imaging upside down, using deep sources and distant observations to image a gridded representation of the seismic reflectivity in the mantle wedge between the source depths and Earth's surface above them.

Basic processing steps (*19*) involved (i) deconvolution of the instrument responses; (ii) deconvolution of the stacked down-going *P*- or horizontally polarized *S*-wave (*SH*) displacement source wavelet from the waveform interval precursory to and including the up-going depth-phase surface reflections (*pP* and *sSH*, where *p* is the up-going *P* wave from the earthquake to the reflector and *s* is the up-going *S*-wave); and then (iii) convolution with Ricker wavelets that had central frequencies of 0.06 Hz (*P*) and 0.05 Hz (*SH*). Each signal was normalized by the strength of the reference *P* or *S* phase, reflected from Earth's surface above the source (*pP* or *sSH*) to eliminate variations in source strength. Corrections were made for path sampling, geometric spreading from the source to the reflector, and radiation-pattern variations between the path to the reflector and the reference phase. We constrained the illuminated region to be in the vicinity of the geometrical ray path to avoid large radiation-pattern corrections; this intrinsically favors the imaging of near-horizontal structures. The normalization of the images by illumination factors and the summing of local dip-angle domain images achieved stable amplitude-balanced migrations (*19*).

The imaging domain extended from 15°S to 25°S, 175°E to 185°E, and from the surface to a depth of 500 km, discretized in 0.1° latitude and longitude increments and 5-km depth increments. About 2300 vertical-component teleseismic *P*-wave seismograms from 85 deep (>400 km) earthquakes with magnitudes larger than 5.0 that occurred between 1988 and 2006 were used, with any signals having weak *pP* arrivals being excluded. Stations at epicentral ranges from 40°

[1]Department of Earth and Planetary Sciences, University of California, Santa Cruz, CA 95064, USA. [2]Energy and Environment Directorate, Institute of Geophysics and Planetary Physics (IGPP), Lawrence Livermore National Laboratory (LLNL), Livermore, CA 94551, USA.

*To whom correspondence should be addressed. E-mail: thorne@pmc.ucsc.edu

to 140° were used. About 3100 *SH*-wave seismograms from 99 deep earthquakes were used, excluding any signals with weak *sSH* arrivals.

The image domain above a given source is an expanding cone, with overlapping paths from multiple events providing the redundant sampling needed for stable migration (Fig. 2 and fig. S1). The distribution of teleseismic stations relative to the source region is non-uniform, with concentrations at azimuths to North America and to Eurasia. Thus, the imaging domain was not uniformly sampled, but the illumination-factor normalization balanced the migration images proportionately, although we applied a threshold so that regions of very limited path coverage were not overly enhanced.

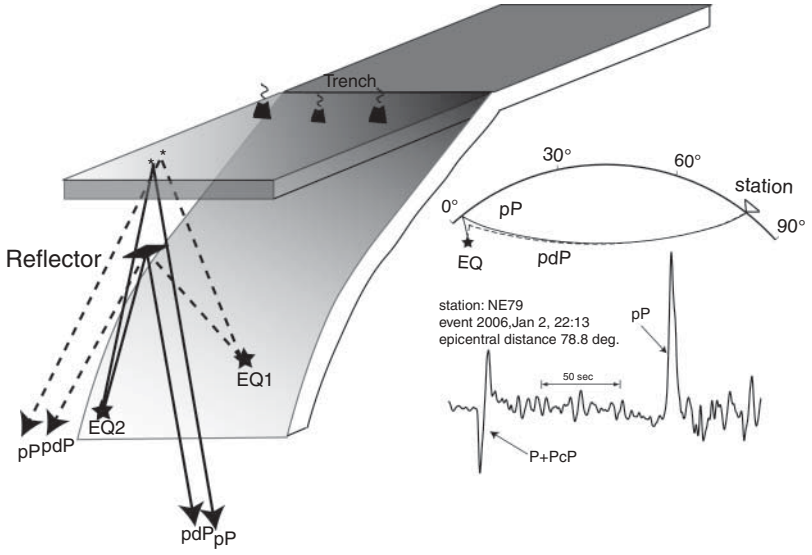

Fig. 1. Schematic of the Tonga mantle wedge imaging geometry. Deep-focus earthquakes within the subducted Pacific plate in the Tonga subduction zone radiate up-going energy that reflects from the underside of Earth's surface (*pP*) or the underside of velocity contrasts at depth *d* above the sources (p_dP) and then travels to teleseismic distances. The p_dP arrivals are precursors to the surface reflections. The inset shows ray paths for p_dP and *pP* to a teleseismic distance of 80°. Data from stations in the range from 40° to 140° were used for imaging the wedge. An example of a vertical-component seismogram is shown on the lower right, with energy between *P* and *pP* mainly caused by underside reflections, which arrive as precursors to *pP*. EQ, earthquake; *PcP*, down-going *P* wave that reflected from the core-mantle boundary.

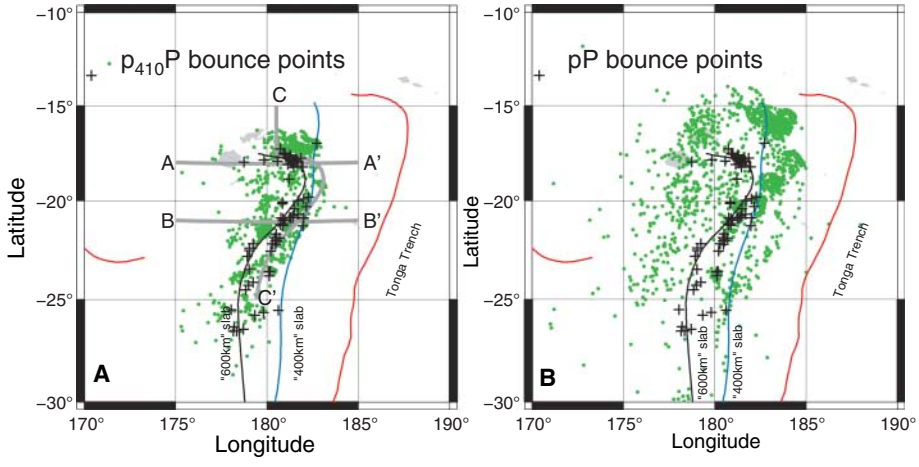

Fig. 2. Map showing earthquake locations (black crosses) and underside geometrical reflection points (green dots) (**A**) at 410 km, $p_{410}P$ and (**B**) at the free surface, *pP*. The positions of the Tonga and New Hebrides trenches are shown in red. The 400-km and 600-km depth contours for the top of the Tonga slab are indicated by the labeled blue and gray lines, respectively. The image volume expands upward toward the surface, with the *pP* surface-reflection points defining the maximum lateral extent of coverage. The locations of the vertical cross sections shown in Figs. 3 and 4 are indicated in (A).

Source depths were taken from a catalog of relocated hypocenters that includes depth phases (*20*) or, for events in 2006, from moment tensor inversions. Random perturbations of the source depths by up to 20 km did not have an important effect on the final migration images. The reference velocity model that we used for the inversions was the 1D model from the International Association of Seismology and Physics of the Earth's Interior (IASP91) (*21*). Minor distortions of the reflectors could occur because of neglect of the 3D volumetric velocity heterogeneity, but no high-resolution *P*- and *S*-wave tomographic models spanning the volume of our image are available for use in the migrations. This led us to emphasize frequencies below 0.1 Hz, so that travel-time decorrelation was not a problem (fig. S2). This bandwidth limited the resolution of the sharpness of the reflectors, but it also ensured that coherent signals stacked to give meaningful images (figs. S3 and S4). The use of multiple events with different focal mechanisms reduces down-going conversions and suppresses receiver-side effects to a great extent.

Confidence bounds on the images were established by performing 200 bootstrap iterations, retaining the same event distribution and total number of traces, while re-sampling the seismogram population. The final images shown are the averaged models, with the color hues saturated for highly resolved (97% confidence) features stronger than 3 SD above background and fading to white for poorly resolved features <1 SD above background (fig. S5).

***P* and *SH* reflectivity**. The migration yielded 3D reflectivity structures with associated variance estimates that are difficult to display in their entirety, so several 2D cross-sectional images are shown (Fig. 3 shows sections mainly along the trend of the Tonga slab; Fig. 4 shows east-west sections through the most densely sampled portions of the image volume, as depicted in Fig. 2). These images convey the primary aspects of the 3D structure (additional cross sections are presented in figs. S6 and S8 to S10). The color scale in Figs. 3 and 4 indicates the strength and sign of the reflected amplitude at each position, relative to the surface reflection, with color saturation decreasing proportional to the number of standard deviations above the noise level. Weak features that are likely to be artifacts are suppressed by this weighting (fig. S5). Because the reference phases were aligned to peak at the free surface, there is a (very saturated) blue stripe right at the surface, underlain by a broader red band that is an artifact caused by the side lobe of the Ricker wavelet. This negative side lobe has an amplitude that is ~40% of that of the positive surface-reflection peak, obscuring any reflectivity above 70 km, such as underside reflections from the crust-mantle boundary. The higher velocity of *P* waves causes the side lobe to broaden more in the *P* images than in the *SH* images. Weak side lobes are also ex-

pected to be present above and below strong arrivals at greater depths.

The reflectivity in the image volume is dominated by quasi-horizontal reflecting surfaces (steeply dipping interfaces, such as the upper boundary of the slab, could not be imaged because of a lack of stations at small epicentral distances), with strong blue features corresponding to *P*- or *SH*-impedance increases with increasing depth and strong red features corresponding to *P*- or *SH*-impedance decreases with increasing depth. Lateral disruptions of the reflectors at large depths occur in poorly sampled regions, underlain by few or no deep earthquakes, but spatial coverage expands upward from the deep sources, so that any lateral continuity is best resolved at shallower depths.

The immediate dominant attribute of the images is that there is extensive *P* and *SH* reflectivity in the Tonga mantle wedge, with extensive lateral continuity. The overall correlation coefficient between all of the *P* and *SH* images is low (with an absolute value of <0.13), but variable illumination and resolution of the structures must be considered. Some features correlate well, whereas others have the opposite sign or no correlation. Specifically, the *P*- and *SH*-wave images consistently show positive reflectors near depths from 75 to 100 km (we refer to this as the "90-km" feature), 300 km, and 410 km. Negative *P* and *SH* reflectors are seen near 330 and 450 km. In the eastern part of the wedge, a *P* reflector near 125 km is negative, but an *SH* reflector is positive. In addition, there is a positive *P* reflector near 200 km, accompanied by a weak positive *SH* reflector far away from the slab and a strong negative *SH* reflector near the slab. There is a patchy positive *P* reflector near 250 km with little *SH* reflectivity, and there is a negative *SH* reflector near 390 km with little *P* reflectivity. For both *P* and *SH* waves, the 410-km reflector becomes more shallow by tens of kilometers in the vicinity of the subducting slab (Fig. 4 and fig. S6). Other boundaries appear to have variable topography and lateral disruptions. In all cases, the apparent depths and apparent topography are probably biased by the use of a laterally homogeneous 1D background model for the migrations. Some other intermittent features are seen in the images, but we believe that our data set robustly resolves only the structures noted above.

Some of the reflectivity features in the Tonga wedge correspond to structures detected in other regions. The strong positive *SH* reflections and weak positive *P* reflections from near 90 km may represent the Hales discontinuity (*22*, *23*). The positive *P* reflector near 200 km may correspond to a feature commonly found under continental regions

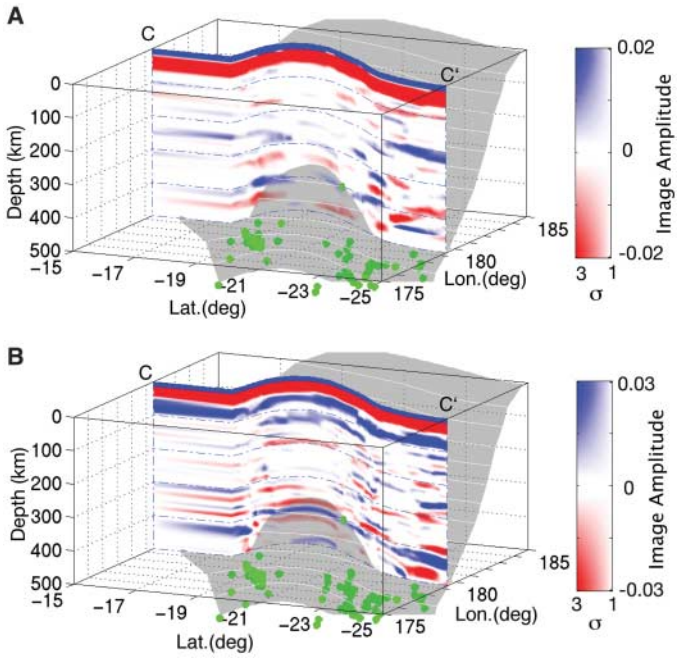

Fig. 3. (**A**) *P*-wave and (**B**) *SH*-wave profiles along vertical section C to C′ (Fig. 2) through the migration volumes. The period of the Ricker wavelet applied to the data is 16 s for *P* and 20 s for *SH*. Blue indicates positive impedance contrasts with increasing depth, whereas red indicates negative impedance contrasts with increasing depth. The color hues are saturated for features >3 SD (3σ) above the background level and fade to white for features <1 SD above the background. The strong blue and red stripes near the surface are the images of the *pP* and *sSH* surface reflections. The upper surface of the subducting Pacific plate is indicated by the gray facade. The deep-focus earthquake hypocenters are shown by green dots. Lat, latitude; Lon, longitude; deg, degrees.

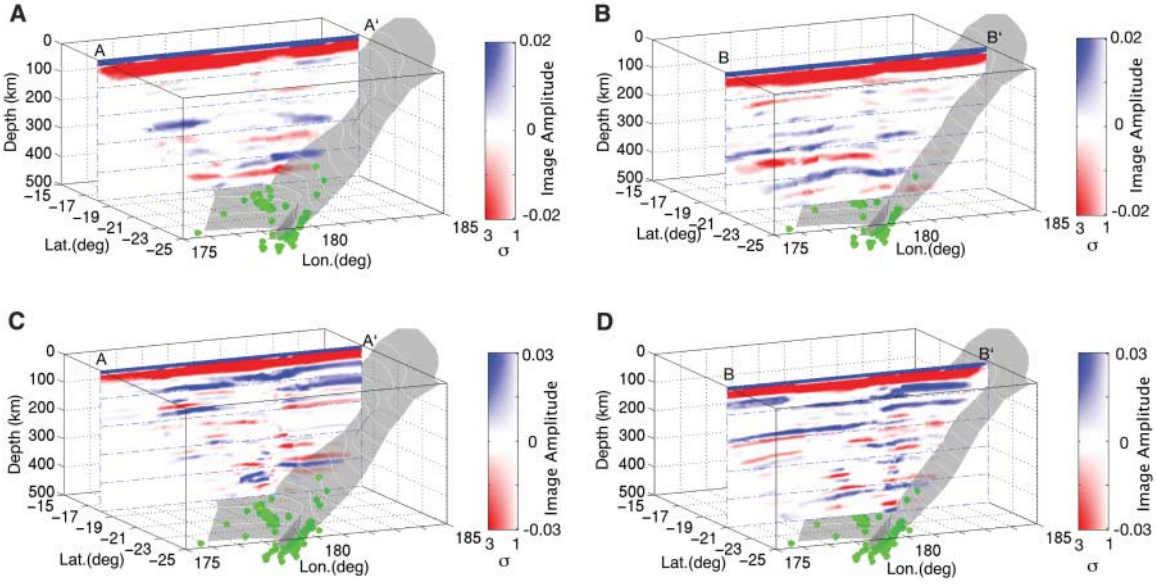

Fig. 4. Vertical west-east profiles in the (**A** and **B**) *P*-wave migration volume and (**C** and **D**) the *SH*-wave migration volume along profiles A to A′ (Fig. 2) at 18°S [(A) and (C)] and B to B′ at 21°S [(B) and (D)]. The period of the Ricker wavelet applied to the data is 16 s for *P* and 20 s for *SH*. Color scales correspond to those in Fig. 3. The strong blue and red stripes near the surface are the images of the *pP* and *sSH* surface reflections. The upper surface of the subducting Pacific plate is indicated by the gray facade. The deep-focus earthquake hypocenters are shown by green dots. The intermittence in the reflectors may be due to non-uniform ray path sampling. In many instances, the reflectors extend to the westward edge of our field of illumination.

(*22*, *24*, *25*) but also seen in back-arc (*23*) and oceanic (*26*) regions. The velocity increase near 300 km observed near 21°S (profile B to B′ in Fig. 4) has been seen in some back-arc and oceanic regions (*23*, *27*), and a weak increase near this depth has been reported along the Tonga arc (*22*) and in a 2D profile across our image volume near 18°S latitude (*10*). The sharp drop in velocity just above the 410-km increase that we find in *SH* images has been detected under continents (*28*, *29*). The 410-km increase is observed globally and regionally (*17*, *22*, *30*), and we consistently observe this in regions where the deep-focus events are concentrated and the up-going phases sample this depth range well.

Thermal and petrological interpretations. The notion of a simple homogeneous upper-mantle corner-flow regime dominated by temperature variations relative to the slab, as typically invoked in textbook cartoons of mantle-wedge processes, is clearly inadequate. The rough structure in the Tonga mantle wedge requires multiple reflecting contrasts in material properties in the wedge that need dynamical and petrological explanations. The bands of reflectivity in our images are not artifacts of wavelet side lobes or other processing effects, but they emerge from the extensive stacking of signals from different source depths and locations. Therefore, we believe they represent true structures, albeit ones that are possibly unique to this back-arc environment. Although corner flow and upwellings under the arc and back-arc basin must involve thermal heterogeneity, this reflectivity requires processes that sharpen the gradients in structure enough to reflect seismic waves, and this suggests petrological effects involving compositional differences, phase changes, partial melt, or anisotropic fabrics.

Standard Earth models predict relatively little upper-mantle reflectivity between 50 and 500 km: A velocity decrease is sometimes observed at the top of a low-velocity zone (the so-called Gutenberg discontinuity found near 65 km depth under oceanic regions), a 220-km velocity increase is primarily associated with continental regions, and the 410-km increase is typically interpreted as the olivine-to-wadsleyite (β-phase) transformation in $(Mg,Fe)_2SiO_4$. Relatively simple upper-mantle structures of this type are at odds with the observation of additional discontinuities in many regions (*22*, *23*, *31*).

The geochemical characteristics of the Lau Basin are notably complex and provide possible insights into the origin of some of the seismic layering in this region. In particular, both sediment-derived melts (*32*) and pervasive slab-derived fluids appear to have altered this region (*33*). When coupled with the observation that hydrous silica-rich melts may be critically important in the subarc mantle (*34*), the possible phase transitions and compositional zonation that might occur within a heavily metasomatized mantle emerge as potential explanations for the seismically layered Tonga mantle wedge. With the rapid eastward rollback of the trench in this region and the exposure of this region to subduction from the former Vitiaz slab (*5*), pervasive metasomatism is expected throughout the entire region of our study. Metasomatically associated mineralogic variations and transitions are thus consistent with the extended lateral continuity of the velocity contrasts we observed (Fig. 4). The spatial distribution of mineralogic heterogeneity associated with metasomatic alteration in the wedge is likely to be complex: Silica enrichment can occur through reactions between ascending liquids and ambient mantle (*35*), residue from solidified melts could be advected downward by corner flow, and lenses of mineralogic heterogeneities could be generated (*36*). In this context, mineralogic components that can produce detectable seismic contrasts (even in small abundance) include albite and silica, each of which undergoes phase transitions with large changes in elastic properties. The former is the dominant component of the trondhjemitic magmas that are likely to be derived from the slab (*34*). If these magmas react with the wedge, they can generate sodic amphibole and highly Mg-rich pyroxene; if they are spatially localized, they can give rise to veins of sodic metasomatic minerals. At ~2.5 GPa and 1000°C, albite decomposes to jadeite and quartz (*37*), with an increase in velocity at the transitions of ~23 and ~29% in *P*- and *S*-wave velocity, respectively (*38*). Accordingly, if even 5% by volume of sodic feldspar is present, seismic velocity increases of ~2% in *P*-wave velocity and ~3% in *S*-wave velocity should occur near 80 km depth (calculated using a Reuss average and assuming equal temperature dependences of the elasticity of each phase).

The key point is that modest quantities of minerals with phase transitions associated with major changes in elasticity can produce weak but resolvable seismic discontinuities, and a heavily altered mantle wedge is certainly mineralogically complex. Free silica could be generated in and subsequently advected throughout the wedge by basaltic liquid emplaced at depth and crystallizing as eclogite, by silica veining associated with aqueous fluids, or by crystallization of trapped silica-rich magmas (such as trondhjemites) at depth. Not only can free silica generate a discontinuity near 90 km depth associated with the quartz-coesite transition, but several percent of silica can generate *P*- and *S*-impedance increases of a few percent near 300 km depth, as a result of the coesite-stishovite phase transition (*27*). Another type of mechanism, the reaction of forsterite and periclase to anhydrous phase B (which involves the depletion of silica), may be an alternative explanation for discontinuities in the 275- to 300-km depth range (*39*). The presence of SiO_2 would decrease the V_p/V_s ratio (where V_p is *P*-wave velocity and V_s is *S*-wave velocity), so a detailed V_p/V_s tomographic map might help to distinguish between these explanations. A recent tomographic study (*7*) showed large decreases (~−0.1) in the V_p/V_s ratio in the depth range of 250 to 350 km beneath the Lau spreading center. This could indicate that free SiO_2 is indeed present.

The positive velocity contrast near 200 km depth may similarly be associated with the interaction of slab-derived siliceous melts with the mantle wedge: Such melts may equilibrate with normal mantle to form Mg-rich orthopyroxene (*34*–*36*), a phase known to undergo a transition near this depth to a high-pressure clinopyroxene structure. In this instance, an ~20% abundance of orthopyroxene would probably be required to generate a velocity contrast of 1 to 2% (*40*). However, abundances of orthopyroxene of near 40% have been observed in metasomatized xenoliths from the mantle wedge underlying the Kamchatka arc (*35*). The lateral variation in the sign of *S* reflectivity near this depth might require a flow-induced change in the anisotropic fabric, possibly a transition from horizontal inflow to slab-parallel downwelling.

The velocity decrease near 330 km depth is near the final depth at which water is anticipated to be released from the basaltic crust, as defined by the high-pressure stability limit of phengite (*41*). This decrease may accordingly define the lower limit of metasomatism and melting (and thus silica enrichment and veining and basalt liquid generation) within the mantle wedge. Stishovite, the stable form of silica at these depths, is ~30% faster than olivine in *S*-wave velocity and almost 40% faster in *P*-wave velocity: A lack of this phase below this depth (and a few percent above it) could generate this decrease in velocity. Although *P*- and *S*-velocities are positively correlated for some features such as the 90-km and 410-km reflectors, the possible range of causes for the structures that we observed does not dictate that they need to be strongly correlated overall. As data accumulate, improved resolution of the reflectivity will be possible.

If mafic melts do become negatively buoyant within the deep upper mantle (*42*), then, depending on their precise chemistry, some melts could descend to above the 410-km-deep olivine-to-wadsleyite transition and produce a thin melt layer, manifested by a sharp *SH*-velocity reduction near 390 km. The observed velocity reduction near 450 km is probably influenced by side lobes of the strong 410-km reflection, but it appears to be too strong to be completely attributed to these lobes. No obvious petrological complexity is anticipated at this depth, but this region may be strongly perturbed by the relic Vitiaz slab remnant, part of which overlies the Tonga slab.

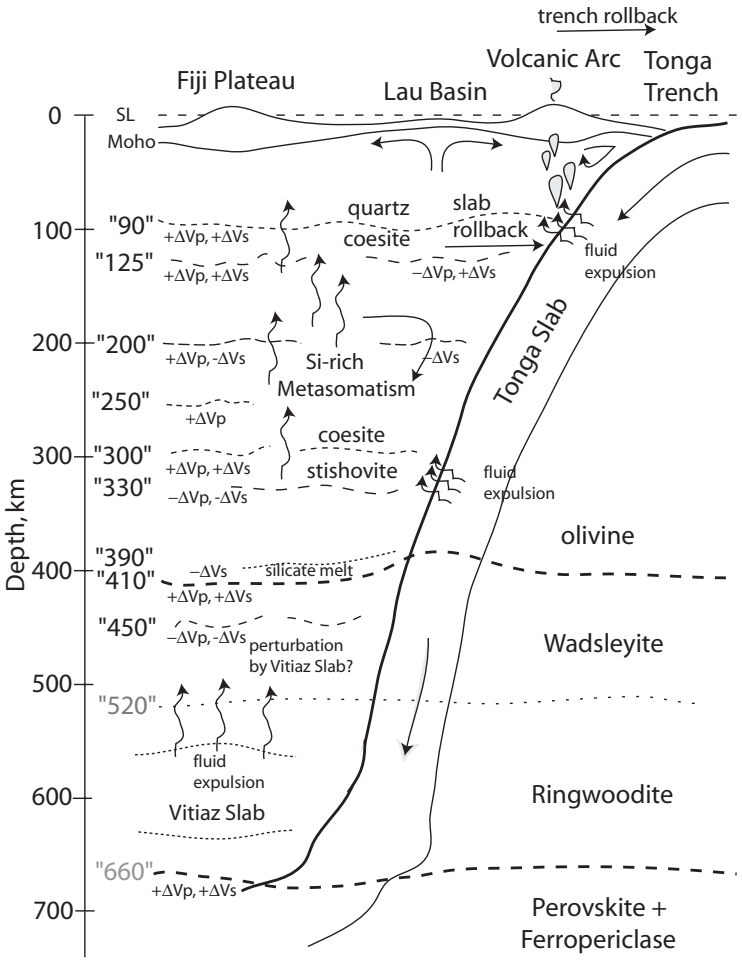

Fig. 5. Schematic cartoon of the Tonga mantle wedge environment above the subducting Tonga slab, highlighting the reflectivity detected in the *P* and *SH* migrations in Figs. 3 and 4. The overall concept is that extensive fluid expulsion has permeated the wedge environment with Si-rich melts and fluids. Fluid expulsion from the slab and possibly from relic pieces of the Vitiaz slab is concentrated at depths near 100 and 325 km. Phase changes in the Si contribute to the reflectivity near 90 and 300 km. The accumulation of silicate melt in a thin layer above the 410-km reflector may have origins in fluid accumulation, and partial melting in the transition zone associated with the perturbed region above the Vitiaz slab may cause reflectivity near 450 km. SL, sea level; ΔV_p, *P*-wave velocity contrast; ΔV_s, *S*-wave velocity contrast.

Fluid expulsion from the slab remnant could possibly lower the velocities or even cause partial melting.

Conclusions. Seismic reflectivity in the mantle wedge between 50 and 500 km was observed to be widespread, and it inspired the creation of a model of an extensively metasomatized region permeated by fluids from the subducted slab (Fig. 5). Given that the wedge is expected to have a complex corner flow, including slab-parallel transport associated with the fan-shaped back-arc spreading of the Lau Basin and slab and trench roll-back, we think it is unlikely that the reflectivity involves strong compositional stratification. Because phase changes of minor components, such as numerous SiO_2-rich veins, can have strong effects on seismic wave velocities, we believe that fluids (and their residues) play a paramount role in both partial melting and the development of the chemical complexity and silica enrichment of the wedge. Shear flows may accentuate the reflectivity by the development of gradients in anisotropic properties. Progress in understanding this very complex environment will require simultaneous consideration of the rough and smooth properties of the medium and not just refined tomographic images.

References and Notes

1. B. R. Hacker, G. A. Abers, S. M. Peacock, *J. Geophys. Res.* **108**, 2029 (2003).
2. K. A. Kelly *et al.*, *J. Geophys. Res.* **111**, B09208 (2006).
3. M. Bevis *et al.*, *Nature* **374**, 249 (1995).
4. M. Gurnis, J. Ritsema, H.-J. van Heijst, S. Zhong, *Geophys. Res. Lett.* **27**, 2373 (2000).
5. W.-P. Chen, M. R. Brudzinski, *Science* **292**, 2475 (2001).
6. D. Zhao *et al.*, *Science* **278**, 254 (1997).
7. J. A. Conder, D. A. Wiens, *Geochem. Geophys. Geosyst.* **7**, Q03018 (2006).
8. E. G. Roth, D. A. Wiens, L. Dorman, J. Hildebrand, S. C. Webb, *J. Geophys. Res.* **104**, 4795 (1999).
9. R. Tibi, D. A. Wiens, *J. Geophys. Res.* **110**, B06313 (2005).
10. H. J. Gilbert *et al.*, *Geophys. Res. Lett.* **28**, 1855 (2001).
11. G. P. Smith *et al.*, *Science* **292**, 713 (2001).
12. R. van der Hilst, *Nature* **374**, 154 (1995).
13. X. Li, S. V. Sobolev, R. Kind, X. Yuan, C. Estabrook, *Earth Planet. Sci. Lett.* **183**, 527 (2000).
14. L. Chen, L. Wen, T. Zheng, *J. Geophys. Res.* **110**, B11310 (2005).
15. J. E. Vidale, H. M. Benz, *Nature* **356**, 678 (1992).
16. Z. Zhang, T. Lay, *J. Geophys. Res.* **98**, 4389 (1993).
17. M. P. Flanagan, P. M. Shearer, *J. Geophys. Res.* **103**, 21165 (1998).
18. Y. Zheng, T. Lay, *J. Geophys. Res.* **111**, B01305 (2006).
19. Additional details of the processing steps are available as supporting material on *Science* Online.
20. E. R. Engdahl, R. D. van der Hilst, R. P. Buland, *J. Geophys. Res.* **88**, 3247 (1998).
21. B. L. N. Kennett, E. R. Engdahl, *Geophys. J. Int.* **105**, 429 (1991).
22. J. Revenaugh, T. H. Jordan, *J. Geophys. Res.* **96**, 19781 (1991).
23. A. Deuss, J. H. Woodhouse, *Geophys. Res. Lett.* **29**, 1249 (2002).
24. J. B. Gaherty, T. H. Jordan, *Science* **268**, 1468 (1995).
25. P. M. Shearer, *Geophys. J. Int.* **115**, 878 (1993).
26. S. Rost, M. Weber, *Geophys. J. Int.* **147**, 12 (2001).
27. Q. Williams, J. Revenaugh, *Geology* **33**, 1 (2005).
28. J. Revenaugh, S. A. Sipkin, *Nature* **369**, 474 (1994).
29. T.-R. A. Song, D. V. Helmberger, S. P. Grand, *Nature* **427**, 530 (2004).
30. E. G. Roth, D. A. Wiens, *Geophys. Res. Lett.* **26**, 1223 (1999).
31. D. L. Anderson, *Tectonophysics* **416**, 7 (2006).
32. S. Turner, C. Hawkesworth, *Nature* **389**, 568 (1997).
33. A. J. R. Kent, D. W. Peate, S. Newman, E. M. Stolper, J. A. Pearce, *Earth Planet. Sci. Lett.* **202**, 361 (2002).
34. G. Prouteau, B. Scaillet, M. Pichavant, R. Maury, *Nature* **410**, 197 (2001).
35. S. Arai, S. Ishimaru, V. M. Okrugin, *Isl. Arc* **12**, 233 (2003).
36. A. Zanetti, M. Mazzucchelli, G. Rivalenti, R. Vannucci, *Contrib. Mineral. Petrol.* **134**, 107 (1999).
37. A. L. Boettcher, P. J. Wyllie, *Contrib. Mineral. Petrol.* **17**, 224 (1968).
38. J. D. Bass, in *A Handbook of Physical Constants*, vol. 2, T. J. Ahrens, Ed. (American Geophysical Union, Washington, DC, 1995), pp. 45–63.
39. J. Ganguly, D. J. Frost, *J. Geophys. Res.* **111**, B06203 (2006).
40. J. Kung *et al.*, *Phys. Earth Planet. Inter.* **147**, 27 (2004).
41. M. W. Schmidt, S. Poli, *Earth Planet. Sci. Lett.* **163**, 361 (1998).
42. A. Suzuki, E. Ohtani, *Phys. Chem. Miner.* **30**, 449 (2003).

43. We thank D. L. Anderson for helpful discussions, P. Shearer and anonymous reviewers for helpful suggestions, and D. Wiens for kindly providing a copy of his 3D tomographic model. This is contribution University Collaborative Research Program grant UCRL-JRNL-229379, supported in part by IGPP-LLNL mini-grant 05-GS-016 and NSF under grants EAR-0125595, EAR-0310342, and EAR-0453884. Seismic data were obtained from the Incorporated Research Institutions for Seismology Data Management Center.

Supporting Online Material

www.sciencemag.org/cgi/content/full/1138074/DC1
Materials and Methods
Figs. S1 to S10

28 November 2006; accepted 27 March 2007
Published online 12 April 2007;
10.1126/science.1138074
Include this information when citing this paper.